

# Dynamic Simulator and Controls for a PEM Fuel Cell Power System

Song-Yul Choe\*

Controls of a PEM fuel cell stack are one of the crucial issues for securing efficient and durable operations of the stack. When the air is excessively supplied, the efficiency of the system drops. Conversely, insufficient supply of the air causes oxygen starvation at a dynamically varying load. In particular, proper cooling strategy ensures rejecting heat produced and prevents any thermal stress on thin layers of cells. Excessive cooling decreases the working temperature and consequently drops efficiency of the stack. In contrast, the thermal stress imposed by insufficient cooling may reduce the lifespan of the layers.

Design of controls needs a model for the plant that sufficiently represents its dynamics. Current models available are either empirical or computationally intensive, which do not allow for analysis of a stack behavior and associated controls. The paper addresses development of a high dynamic model for a stack that is based on transport of charges, flow of fuels and byproducts taken into temperature effects. The stack is constructed with single cells composed of sandwiched multiple layers that are thermally and electrically coupled. Air is supplied by a blower, which voltage is regulated. Two representing control strategies for the air supply system are designed and compared. Heat is rejected by a thermal circuit that consists of a pump, a three-way valve, and a radiator with a fan and a reservoir. In order to control the coolant flow rate, a linear cascade and a state feedback control are designed and compared, which includes a feed-forward function that is derived from load profile. In addition, the temperature effect on air flow rate is compensated, so that a deviation of the oxygen excess ratio can be suppressed.

The dynamics and performance of the designed controllers are evaluated and analyzed by simulations using dynamic fuel cell system models at a multi-step current and a current profile measured at the Federal Urban Driving Schedule. The results show that the control strategy proposed reduces not only temperature rise in the catalyst layer but also the parasitic power needed for operation of the air and coolant pumps maintaining the oxygen excess ratio set.

**Keywords:** PEMFC, Dynamic Models, Air Supply System, Thermal Circuit, Controls

## NOMENCLATURE

<i>Alphabets:</i>			<i>M</i>	<i>Molar mass</i>	$kg\ mol^{-1}$
<i>A</i>	<i>Area</i>	$m^2$	<i>N</i>	<i>Mole flux</i>	$mol\ s^{-1}m^{-3}$
<i>B</i>	<i>Membrane extension</i>		<i>n</i>	<i>Number</i>	
<i>C</i>	<i>Coefficient</i>	$kg\ m^{-3}$	<i>p</i>	<i>(partial) Pressure</i>	$Pa$
<i>C<sub>p</sub></i>	<i>Specific heat</i>	$J\ kg^{-1}\ K^{-1}$	<i>Q</i>	<i>Heat transfer</i>	$J$
<i>F</i>	<i>Faraday number</i>	$A\ s\ mol^{-1}$	<i>R</i>	<i>Universal gas constant</i>	$J\ kg^{-1}\ K^{-1}$
<i>Fr</i>	<i>Radiator frontal area</i>	$m^2$	<i>R</i>	<i>Resistance</i>	$\Omega$
<i>i</i>	<i>Current density</i>	$A\ m^{-2}$	<i>s</i>	<i>Entropy</i>	$J\ mol^{-1}K^{-1}$
<i>h</i>	<i>Heat transfer coefficient</i>	$W\ m^{-2}\ K^{-1}$	<i>t</i>	<i>Thickness</i>	$m$
<i>J</i>	<i>Rotational inertia</i>	$kg\ m^2$	<i>T</i>	<i>Temperature</i>	$K$
<i>m</i>	<i>Mass</i>	$kg$	<i>W</i>	<i>Mass flux</i>	$kg\ s^{-1}$
			<i>Superscripts, subscripts :</i>		
			<i>amb</i>	<i>Ambient</i>	
			<i>an</i>	<i>Anode</i>	
			<i>bl</i>	<i>Blower</i>	
			<i>c</i>	<i>Coolant</i>	
			<i>ca</i>	<i>Cathode</i>	
			<i>catl</i>	<i>Catalyst layer</i>	

\*Mechanical Engineering Department  
Auburn University, Auburn, AL 36848  
choe@eng.auburn.edu  
Phone: 344-844-3382  
Fax: 344-844-3307

<i>cond</i>	Conduction
<i>conv</i>	Convection
<i>cv</i>	Control volume
<i>diff</i>	Diffusion
<i>elec</i>	Electro
<i>g</i>	Gas
<i>i</i>	Index
<i>m</i>	Motor
<i>membr</i>	Membrane layer
<i>pl</i>	Plumbing
<i>rad</i>	Radiator
<i>res</i>	Reservoir
<i>s</i>	Stator
<i>sou</i>	Source
<i>st</i>	Stack

#### Greek symbols:

$\varepsilon$	Porosity	
$\tau$	Tortuosity, torque	$N\ m$
$\lambda$	Water content, ratio	
$\rho$	Density	$kg\ m^{-3}$
$\omega$	Angular velocity	$rad\ s^{-1}$
$\eta$	Efficiency	
$\varphi$	Flux linkage	$V\ s\ rad^{-1}$

## 1. INTRODUCTION

The PEM fuel cell is a chemical device that generates electrical power and ejects heat and water (i.e. oxygen and hydrogen) as byproducts of the chemical reaction. Thus, the fuel cell is regarded as being free of air pollution, whose advantages let the PEM fuel cell be considered as a potential and alternative energy source in future automotive and stationary applications.

To replace the conventional power sources, the fuel cell systems must be analyzed and evaluated for performance, efficiency and reliability. The properties of PEM fuel cells are interrelated with factors including transport of reactants and byproducts, management of heat generated by electrochemical reaction or by current passing through the cell, and control of humidity to maintain adequate electrolyte conductivity [1].

The balance-of-plant (BOP) is a group of system components that supply reactants, remove generated heat, manage produced water and control actuators. Typical components needed for operating a PEM fuel cell system are a hydrogen tank to store fuel, an air compressor or blower along with inlet/outlet manifold, and a humidifier to supply humidified oxygen, and a bypass valve, a radiator with a fan, a reservoir, a coolant pump, and several control valves and controllers to properly manage the heat generated. A typical configuration is shown in Figure 1.

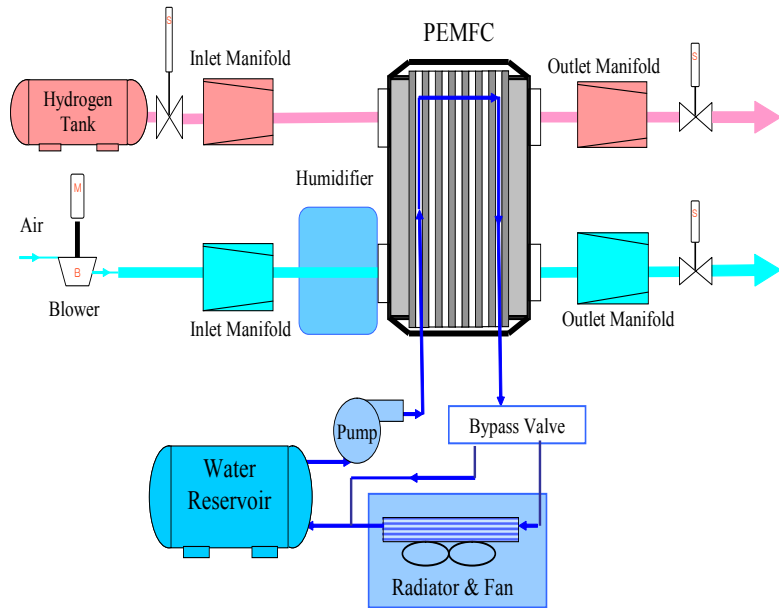


Figure 1: A schematic diagram of a PEM fuel cell system

## 2. MODELING OF PEM FUEL CELL SYSTEM

Controlling of a fuel cell power system requires a better understanding of the dynamic behavior of the stack that interacts with different BOP components. Due to the complexity of the system, dynamic models are utilized to efficiently design and effectively assess controllers. In the following chapters, the models for the PEM fuel cell stack, air supply and thermal system are described.

### 2.1 Fuel Cell Stack

Most fuel cell models, which describe physical behaviors of a PEM fuel cell, are based on either empirical equations fitted to the curve of a specific polarization characteristic [2] or the CFD (Computational Fluid Dynamics) to solve the mass and charges transport [3][4][5]. The former has been proposed for designing a controller for the air supply system. The dynamics lacking in a cell are improved by reflecting the charging and discharging behavior of the double layer present on the interface between electrodes and electrolytes. However, the model does not fully include the dynamics of gas and temperature occurring through the flow paths and in the cell when the current is applied. In addition, the partial pressure drops along the pores in the GDL that affect the net pressure exerted on the chemical reaction rate and increase the over-potential, are not considered. The temperature rise that eases water removal, increases the chemical reaction and subsequently affects the output voltage of a cell has not

been taken into account.

On the other hand, the CFD based models have been widely employed to analyze transport mechanisms of the mass and charge and their spatial distributions for a single cell, but limited to represent the dynamic characteristic of a stack in conjunction with components of the BOP and a power system. In addition, exponential growth of computational time required for unsteady analyses impedes application of the model for the stack.

The model used in this paper is based on empirical equations and takes into account three additional major effects – water balance in the membrane, gas dynamics in the gas diffusion layer and temperature distribution in a cell described below.

A cell is constructed by the connection of individual models for layers. The I-V characteristic is obtained through the difference between the open circuit voltage and the over-potentials that include the ohmic over-potential in the membrane, the activation over-potential in the catalyst on the cathode side, and the concentration over-potential. The relationship for a single cell may be written as the function of physical parameters such as the reactant partial pressure, temperature, and current and membrane water content [2]. The output characteristic of the stack is assumed by the product of the cell number with one of a single cell.

$$\begin{aligned} V_{cell} &= E(p, T) - v_{act}(p, T, i) - v_{ohmic}(i, \lambda_{membr}, T) - v_{conc}(p, T, i) \\ V_s &= n \cdot V_{cell} \end{aligned} \quad (1)$$

The dynamics of a fuel cell system involve mass flow of air and water. The air supplied flows through the gas flow channel and the GDL before reaching the catalysts, and at the same time, takes up water from the humidifier. Water generated in the catalysts diffuses through the membrane where protons take up water from the anode to the cathode side. The heat generated by chemical reaction and charge transport elevates temperature in the cell. All of these changes affect the dynamic behavior of the cell. Further improvements of the dynamics have been made by considering the following three effects: 1) Water dynamics in the membrane, 2) Partial pressure drop in the GDL and 3) Temperature variation.

Water content in the membrane determines proton conductivity. The dynamics of water content are described by two effects: the electro-osmotic driving force by the different electrochemical potentials at the anode and cathode, and the diffusion caused by the

water concentration gradient at the two boundaries. Considering the water mass that flows at the boundaries of the membrane layer, the dynamic of the water concentration in the membrane can be improved as follows [6], where  $C$  is the mass concentration ( $\text{kg} \cdot \text{m}^{-3}$ ),  $M$  is the mole mass ( $\text{kg} \cdot \text{mol}^{-1}$ ),  $b$  is the parameter given in reference [7],  $\rho$  is the membrane dry density ( $\text{kg} \cdot \text{m}^{-3}$ ), and  $A_{cell}$  is the fuel cell area ( $\text{m}^2$ ).

$$\begin{aligned} \lambda_{membr} &= \frac{C_{H_2O, mass} / M_{H_2O}}{\frac{\rho_{dry, membr}}{M_{membr}} - b \cdot C_{H_2O, mass} / M_{H_2O}} \\ \dot{m}_{water, membr} &= \frac{d(C_{H_2O, mass} A_{cell} t_{membr})}{dt} \\ &= W_{ele, membr, an} - W_{ele, membr, ca} + W_{diff, membr, an} + W_{diff, membr, ca} \end{aligned} \quad (2)$$

The reactant entering the cell diffuses through the GDL before reaching the catalyst layer, and significantly affects the overall dynamics of the reactants. This diffusion effect is reflected by using the mass continuity and the Stefan-Maxwell equations (3) [8]:

$$\begin{aligned} \frac{\epsilon_g}{RT} \frac{\partial p_i}{\partial t} + \frac{\partial N_i}{\partial y} &= 0 \\ \frac{\epsilon_g}{\tau^2} \frac{\partial p_i}{\partial y} &= \sum_{k=1}^3 \frac{RT}{p_{ca} D_{ik}} (p_i N_k - p_k N_i) \end{aligned} \quad (3)$$

Hence,  $i, k$  (1, 3) sum up the species partial pressures where  $p_1$  is the oxygen partial pressure, and  $p_2 = p_{sat}(T)$  and  $p_3$  are the water vapor and the nitrogen partial pressure, respectively, and the diffusion coefficients of  $p_{ca} D_{ik}$  include the cathode pressure of  $p_{ca}$ . The parameters  $\tau$  and  $\epsilon_g$  are constants describing the pore curvature of the GDL.

If a cell is assembled with cubical layers, in which the thermo-physical properties are isotropic and constant, then according to the energy conservation equation, the total energy changes in a controlled volume are equal to the sum of energy exchange at boundaries and internal energy resources. In fact, the energy exchanges at boundaries occur by two factors: a) the conduction across the cell; b) the convection occurring between bipolar plates with the coolant, reactants and water. The thermal-dynamic behavior can thus be described with the following energy conservation equation (4) [6]:

$$\sum_i C p_i C_{i, mass} A_{cell} t_r \frac{dT_{cv}}{dt} = \underbrace{\sum W_{in} C p_j (T_{in} - T_{cv})}_{\text{mass flow in}} + \underbrace{\dot{Q}_{conv}}_{\text{convection heat transfer}} + \underbrace{\dot{Q}_{cond}}_{\text{conduction heat transfer}} + \underbrace{\dot{Q}_{sou}}_{\text{sources}} \quad (4)$$

The internal energy source is composed of the entropy loss and the chemical energy required for protons to overcome the barrier of the over-potentials in both catalyst layers (6). In addition, others are ohmic losses caused by a transport of electrons and protons in the cell [9]:

$$\dot{Q}_{sou} = I \cdot \left( -\frac{T\Delta s}{4F} + v_{act} + I \cdot R_{membr} \right) \quad (5)$$

where  $\Delta s$  is equal to  $-326.36 \text{ J mol}^{-1}\text{K}^{-1}$  [10],  $v_{act}$  is given in the reference [11] and  $R_{membr}$  is the membrane resistance.

Based on the model described above for the single cell, a model for a 10-cells stack [12] is constructed shown in Figure 2.

A multiple step load current was applied. Dynamic response of individual cell voltages and temperature profile at the 400, 550 and 800 seconds is shown in Figure 3.

The amplitude of the overshoot of the output cell voltage strongly depends on the temperature. An analysis shows that a sudden temperature drop with a high current causes high amplitude of the overshoot. Conversely, the influence of temperature on the voltage overshoot becomes less at the low current step because the heat produced is more effectively extracted under the same condition of the coolant.

In addition, the waveform of voltage of the 10 cells does not have the same tendency but fluctuates with distortions at special operating conditions. For example, the output voltage of the 2nd cell at an instant can be higher than the 5th cell expected with the highest voltage. The open circuit voltage (OCV) is a function of the temperature whose derivative shows a negative value. Therefore, the OCV decreases when the temperature rises. Consequently, the voltage of the 2nd term of the OCV is higher than that of the 5th.

Furthermore, the high temperature causes more water to be stored as vapor at the electrodes. Particularly, the 2nd cell has lower temperature than the one in the 5th, which leads to less water vapor. The concentration of oxygen becomes larger and the associated over-potential does smaller.

## 2.2 Air Supply System

The air supply system should continuously replenish the air to the fuel cell stack as the load varies. It consists of four subsystems: an air supplier, a humidifier, and an inlet and outlet manifold with a regulator adjusting

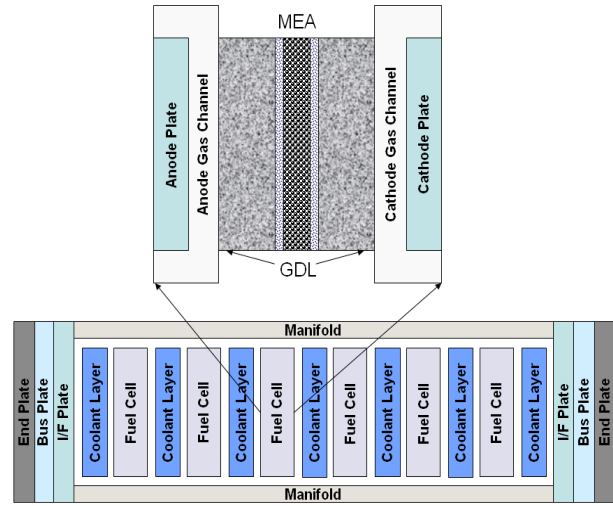


Figure 2: Stack schematic configuration

the pressure at the stack.

Due to the efficiency of the system, a blower is widely employed for supplying air [13]. The humidifier in the study is simplified as an ideal one without any associated dynamics and energy losses.

The blower is usually driven by an electric motor. The dynamic characteristic of the blower system is described by a sum of all moments of inertia of the motor and the impeller, and the torque produced by the motor. Hence, the torque produced by the motor,  $\tau_{bl,m}$  (J), is a function of the stator resistance,  $R_{s,bl,m}$  (Ohm), flux linkage,  $\Phi_{bl,m}$  (V s rad<sup>-1</sup>), and the number of the poles,  $n_{bl,m,pl}$ , with the stator voltage,  $V_{bl,m}$  (V) [7].

$$\frac{d\omega_{bl}}{dT} = \frac{1}{J_{bl}} \left( \tau_{bl,m} - \frac{W_{bl} \Delta P_{bl} \eta_{bl,m}}{\eta_{bl} \rho_{amb} \omega_{bl}} \right)$$

$$\tau_{bl,m} = \eta_{bl,m} \frac{3}{2} \left( \frac{n_{bl,m,pl}}{2} \right) \left( \frac{\Phi_{bl,m}}{R_{s,bl,m}} \right) \left[ V_{bl,m} - \left( \frac{N_{bl,m,pl}}{2} \right) \Phi_{bl,m} \omega_{bl} \right] \quad (6)$$

where  $\omega$  is angular velocity (rad s<sup>-1</sup>),  $J$  is rotational inertia (kg m<sup>2</sup>),  $\eta$  is efficiency,  $p$  is pressure (Pa), and  $\rho$  is air density (kg m<sup>-3</sup>). The flow rate of the air blower is given as a function of the angular velocity and pressure and the efficiency as a function of the flow rate and the angular velocity [14]:

$$W_{bl} = \begin{cases} \omega_{bl} \cdot \left( -20.581 \cdot (p^*) - 1.4415 \cdot 10^{-3} \cdot p^* + 4.1333 \cdot 10^{-5} \right) p^* \leq 9 \cdot 10^{-4} \text{ Pa} \cdot \text{s}^2 / \text{rad}^2 \\ \text{otherwise, } \omega_{bl} \cdot \left( -1.7973 \cdot p^* + 1.6409 \cdot 10^{-3} \right) \end{cases} \quad (7)$$

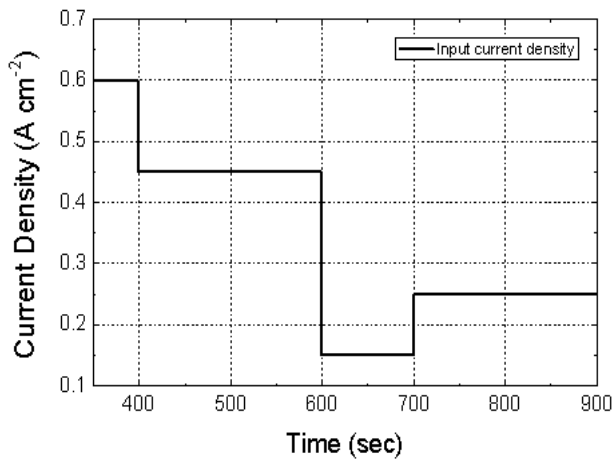


Figure 3a: Step current input

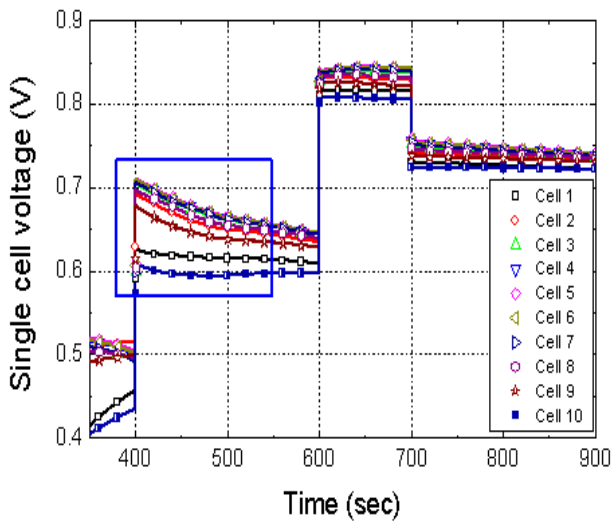


Figure 3b: Dynamic voltage output of the 10 cells

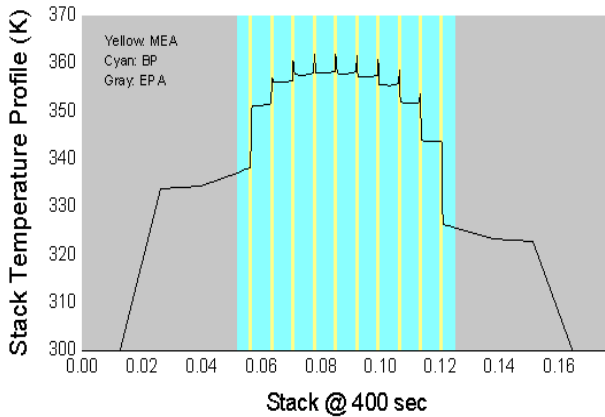


Figure 3c: Stack temperature distribution at the 400 second

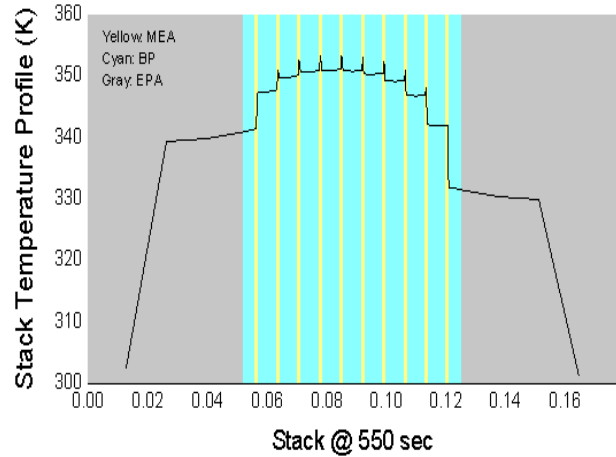


Figure 3d: Stack temperature distribution at the 550 second

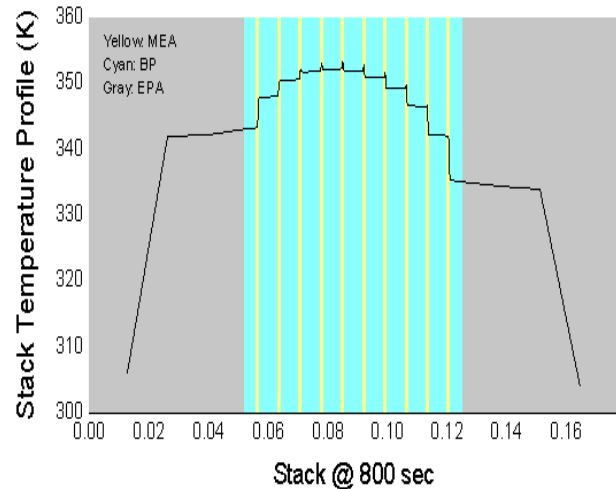


Figure 3e: Stack temperature distribution at the 800 second

$$\eta_{bl} = -2.8831 \cdot 10^{-3} \cdot \left(\frac{W_{bl}}{\Omega_{bl}}\right)^3 + 9.5115 \cdot 10^{-8} \cdot \left(\frac{W_{bl}}{\Omega_{bl}}\right)^2 + 1.3087 \cdot 10^{-4} \cdot \left(\frac{W_{bl}}{\Omega_{bl}}\right) + 0.17945 \quad (8)$$

where  $p^*$  is  $\left(\frac{p_{ca} - p_{amb}}{\Omega_{bl}^2}\right)$ .

The parameters of the blower are extracted by characteristic data and specifications delivered by PADT (Phoenix Analysis & Design Technologies) [15], which include both the flow parameter and overall efficiency versus the head parameter.

Dynamic characteristic of the inlet and outlet manifold

pressures are described by using the mass conservation equation.

$$\frac{dp_{im}}{dt} = \frac{\gamma R_a}{V_{im}} (W_{bl} T_{bl} - W_{im,out} T_{im})$$

$$\frac{dp_{om}}{dt} = \frac{R_a T_{om}}{V_{om}} (W_{ca,out} - W_{om,out})$$

### 2.3 Controls of Air Flow Rate

Block diagram for the controls that includes two conventional PI controllers for controlling the flow rate of the air and the coolant is depicted in Figure 4. Different control strategies for the air supply system are proposed by Pukrushpan et al. [16]. The objectives for the control are to maintain the optimal oxygen excess ratio and subsequently to prevent an oxygen starvation that may occur during abrupt changes of the load current. Hence, the oxygen excess ratio is defined as a rate of oxygen supplied to the consumed.

Two control strategies, a static feed-forward (SFF) and a static feed-back (SFB), have been designed for the system and compared in Figure 6. The principle of SFF uses a polynomial that interpolates map data that includes an optimal relationship between the stack current required and the motor voltage of the blower in order to maintain the oxygen excess ratio at 2, provided that the air flow of the blower can be simply controlled by a motor voltage.

According to simulations, the SFF shows an excellent dynamic behavior at the rejection of the disturbance, but still has a steady state error. The errors can be fully removed by employing a feedback controller shown in Figure 4, called SFB. The principle of the SFB is based on compensation of the blower motor voltage by the use of a PI controller that amplifies the deviation between the actual state values and the state values at a given stack current used for the SFF. In fact, the stack with the air supply system can be described by differential equations, which include nonlinear terms. Therefore, the nonlinear equations are linearized at an operating point: the stack current,  $w^o = I_{st} = 258 A$ , the blower motor voltage,  $u^o = v_{bl}^{opt} = 118V$ , and an oxygen excess ratio,  $\lambda_{O_2}^{opt} = 2$ .

As a result, the linear equations are obtained and expressed with a general form as (Equation 10):

$$\begin{aligned} \delta \dot{x} &= A \delta x + B_u \delta u + B_w \delta w \\ \delta y &= C_y \delta x + D_{yu} \delta u + D_{yw} \delta w \\ \delta z &= C_z \delta x + D_{zu} \delta u + D_{zw} \delta w \end{aligned} \tag{10}$$

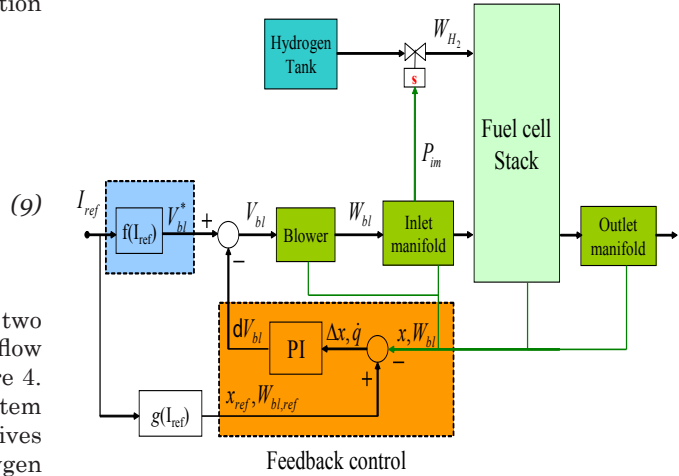


Figure 4: Block diagram of feedback controls for air flow rate

where  $\delta$  denotes the derivative operator at an operating point. The variables of the fuel cell system can be defined as:

$$x = [m_{O_2} \ m_{H_2} \ m_{N_2} \ \omega_{bl} \ p_{im} \ m_{im} \ m_{w,an} \ p_{om}] \quad (States)$$

$$u = V_{bl} \quad (Controlled\ input)$$

$$w = I_{st} \quad (Disturbance)$$

$$y = [W_{bl} \ p_{im} \ V_{st}] \quad (Output)$$

$$z = [P_{net} \ \lambda_{O_2}] \quad (Performance\ variables)$$

The matrices values of the linearized system including  $A, B_u, B_w, C_y, D_{yu}, D_{yw}, C_z, D_{zu}$  and  $D_{zw}$  are listed in the Appendix. The units used for state and output variables are:  $m$  (g),  $p$  (bar),  $\omega$  (kRPM),  $W$  (g/sec),  $P$  (kW),  $V$  (v) and  $I$  (A).

The gains of the PI controller for the SFB are optimized by using the LQR (Linear Quadratic Regulator) [17]. A new state variable,  $\dot{q}$ , is defined, which represents the error of the air flow rate resulting from the deviation of the states. Thus, the PI controller should reflect the error of the flow rates along with the deviation of the state variables:

$$\dot{q} = W_{bl} - W_{bl,ref} \tag{11}$$

The final motor voltage can be obtained by the following equation with a control input,  $u (= V_{bl})$ :

$$u = u^* - K_p \cdot \Delta x - K_I \cdot q \tag{12}$$

where  $\Delta x$  denotes the state errors,  $u^*$  the optimal blow voltage to give the desired air flow rate,  $K_p$  and  $K_I$  are the gains for the controller.

The gains for the PI controller are optimized by using the LQR. If the cost function,  $J$  (Equation 13) is a minimum value, the gains become optimal.

$$J = \int_0^{\infty} (\delta z_2^T Q_z \delta z_2 + q^T Q_I q + \delta u^T R \delta u) dt \tag{13}$$

where  $Q_z$  and  $Q_I$  represents the weighting factors amplifying the errors of the control objects, while the other weighting matrix  $R$  is used to suppress effects of the manipulating variable. Responses of the oxygen excess ratio on different weighting factors are shown in Figure 5.

According to studies, the weighting factor  $Q_I$  only influences the flow rate error,  $q$ , and the integrator gain in the second term of the cost function. When  $Q_I$  increases, the overall influence of the second term in the cost function gets larger. Therefore, the rest terms in the function become smaller at a minimal value of the function. In fact, the variables  $\delta z_2$  is a function of state variables,  $C_z \cdot \delta x$ . As a result, the decreased  $\delta z_2$  leads to an increase in the error that cannot be compensated by the proportional controller. At the same time, the influence of the integrator increases. Consequently, the dynamic response of the recovery behavior of the oxygen excess ratio gets faster, but shows an overshoot before settling into a steady state.

Conversely, the weighting factor  $Q_z$  hardly improves

the transition behavior. The optimum values of the weighting factors are determined with  $Q_z = 1$  and  $Q_I = 0.01$ , which results in the following gains for the PI controller:

$$K_p = \begin{bmatrix} 1.1060 \cdot 10^5 & 0 & -1.2636 \cdot 10^5 & 20.717 & 2.7681 \cdot 10^3 & -0.0019 & 0 & 3 & .5587 \end{bmatrix}$$

$$K_I = -3.1623 \tag{14}$$

Figure 6 shows a comparison of responses of the SFF and the SFB on a multiple-step current, where the SFB improves the rejection dynamics on the disturbance the instant the step current changes. In addition, the excursion of the oxygen excess ratio is also reduced with the SFB.

### 2.4 Thermal Circuit

All previous designs assumed the working temperature of the cell as a constant. As a matter of fact, the temperature in the stack varies because of the heat produced by irreversible energy occurring in the chemical reactions, and Joule's losses associated with charges transport.

A thermal circuit should be capable of rejecting excessive heat produced by the stack. The circuit consists of a three-way valve to allow the coolant to bypass or to flow into a radiator to exchange heat with the ambient media, a fan to increase effectiveness of the heat convection, and a reservoir to store and thermally insulate the coolants. Finally, a coolant pump serves to supply the coolant for the heat source.

The opening of the bypass valve is assumed to be linear with a factor  $k$ , the coolant temperature at the reservoir inlet is expressed as a function of  $k$ , the coolant temperature at the stack outlet,  $T_{st,c,out}$ , and the radiator outlet,  $T_{rad,c,out}$ .

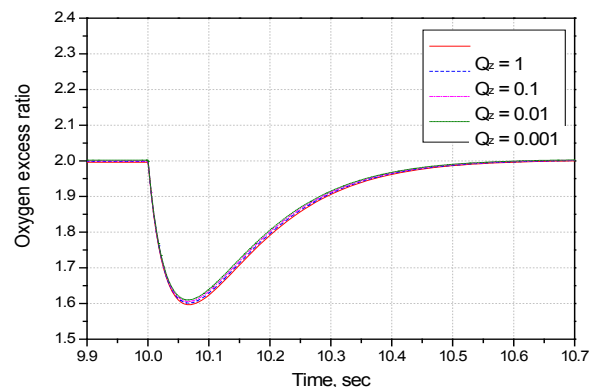
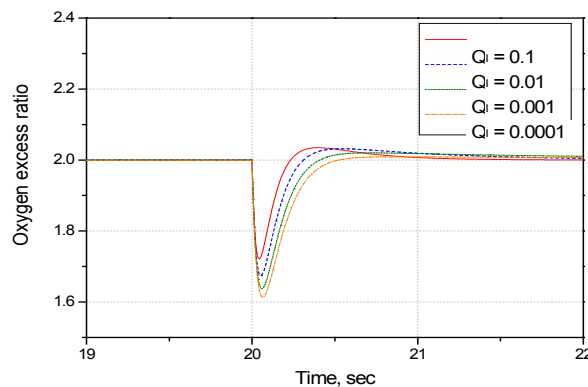


Figure 5: Effect of the weighting factor  $Q_I$  and  $Q_z$  on the recovery behavior of the oxygen excess ratio

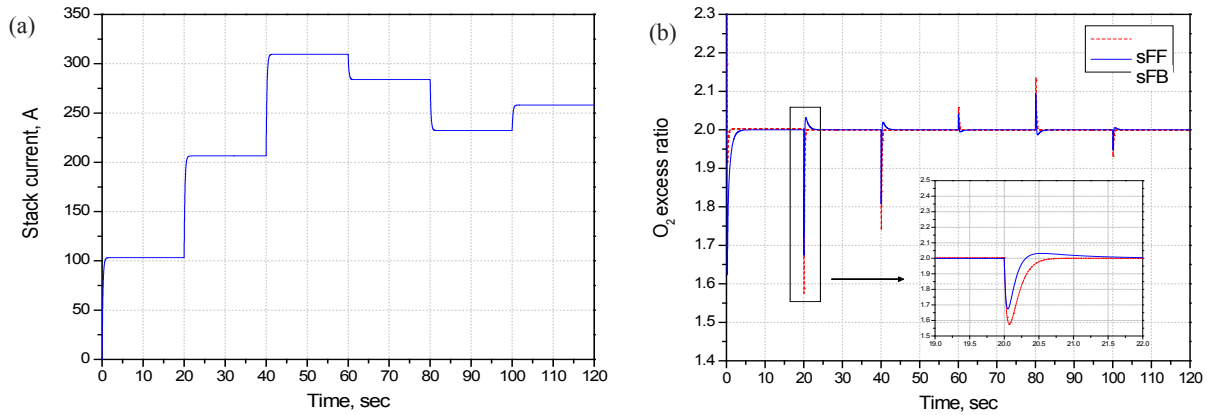


Figure 6: Comparison between SFF and SFB (a) current; (b) oxygen excess ratio at a constant working temperature of the stack

$$W_c \cdot c_p \cdot T_{res,c,in} = (1-k) \cdot W_c \cdot c_p \cdot T_{st,c,out} + k \cdot W_c \cdot c_p \cdot T_{rad,c,out} \quad (15)$$

The behavior of the radiator is described by the principle of thermodynamics. Kroger [18] proposed an empirical equation for a heat transfer coefficient of the radiator,  $h_{rad}$  ( $\text{kW} \cdot \text{m}^{-2} \cdot \text{W}^{-1}$ ) and pressure drop  $p_r$  (kPa) of the radiator as a function of the air flow rate,  $W_{air}$  ( $\text{kg} \cdot \text{s}^{-1}$ ) [9].

$$h_{rad} = -1.4495 \cdot W_{air}^2 + 5.9045 \cdot W_{air} - 0.1157$$

$$p_r = (326.12 \cdot W_{air} - 75.396) + 101.325 \quad (16)$$

If the heat of the coolant is fully transferred to the radiator without any losses, the heat capacity of the coolant is identical with that of the radiator. Thus, the radiator outlet coolant temperature can be expressed as a function of the radiator geometry and the heat convection caused by the temperature difference between the ambient and the radiator outgoing air temperature [9]:

$$T_{rad,c,out} = T_{rad,c,in} - 0.5 \cdot \left( \frac{Fr_{area} \cdot (T_{rad,c,in} - T_{amb}) \cdot h_{rad}}{W_c \cdot c_p} \right) \quad (17)$$

Hence,  $Fr_{area}$  denotes the frontal area ( $\text{m}^2$ ) of the radiator and  $T_{rad,c,in}$  denotes the radiator inlet coolant temperature. The electric power for the fan can be calculated according to a thermal dynamic relationship between pressure drop and air flow rate [9].

$$P_{fan} = \frac{1}{\eta_{elec} \eta_{fan}} \left( W_{air} \cdot C_p \cdot T_{amb} \cdot P_r^{\left( \frac{k-1}{k} \right)} \right) \quad (18)$$

where  $P_{fan}$  denotes the electric power (W) of the fan.

The reservoir should be thermally insulated after a heat exchange at the radiator by convection. The variation of the heat in the reservoir is the sum of the heat that the coolant carries and the heat being exchanged with the ambient. Therefore, the reservoir outlet coolant temperature at the end of the given time interval,  $T_{res,c,out}$  K can be expressed by the equation [9]

$$T_{res,c,out} = T_{res,p} - \frac{\Delta t}{m_{res} \cdot c_p} \left( W_c \cdot c_p \cdot (T_{res,p} - T_{res,in}) \cdot hA_{pl} \cdot (T_{res,in} - T_{amb}) \right) \quad (19)$$

where  $T_{res,p}$  is the temperature of the reservoir at the previous of time step (K),  $\Delta t$  is the time interval (sec),  $m_{res}$  is equivalent to the coolant mass in the reservoir (kg),  $T_{res,c,in}$  is the reservoir inlet coolant temperature (K) and  $h \cdot A_{pl}$  is the heat transfer of plumbing to the ambient ( $\text{J} \cdot \text{K}^{-1}$ ), respectively.

Suppose that all of the heat generated in the stack is completely transferred to the coolant; the coolant flow rate is expressed by the relationship with the heat source [9].

$$W_c = \frac{\dot{Q}_{sou}}{c_p \Delta T} \quad (20)$$

At an equilibrium state, the excessive heat rejected by the coolants is identical to the sum of the heat the reservoir stores and the radiator exchanges with the ambient. Firstly, a maximum coolant flow rate is assumed and then the temperature drop along the coolant flow channel can be calculated by taking into account the fact that the maximum heat produced in the stack should be rejected by the coolant flow rate. The temperature at the outlet of the coolant is assumed to be 72°C because the temperature gradient from the catalyst to the coolants channel amounts to 8° at a maximum load current if the catalyst temperature is 80°C. Thus, the inlet temperature is obtained at a temperature drop of 12°C and the maximum flow rate of 3 kg/sec. The heat transfer coefficient of the radiator and the volume of the reservoir are chosen based on the maximum heat capacity stored and rejected.

**2.5 Coolant Control Strategies**

Block diagram for the air supply system and thermal circuit with different controls is depicted in Figure 7. While the amount of consumed oxygen depends on the stack current, the amount of oxygen supplied to a fuel cell is directly related to the blow motor voltage. Thus, the air supply controller, a static feed-forward controller (SFF) [16], uses a polynomial that interpolates map data that includes an optimal relationship between the stack current required and the motor voltage of the blower in order to maintain the oxygen excess ratio at 2. Then, the air flow of the blower can simply be controlled by a blower motor voltage. The design of such a control is extensively handled by other authors [19] [20] [21]. As shown in Figure 6, the rejection behavior of the oxygen excess ratio at a disturbance can be optimized by the controllers. However, it is assumed that the working temperature of the stack is constant. The objectives for the feedback loop of the air supply system are to

maintain the optimal oxygen excess ratio and prevent an oxygen starvation that may occur during abrupt changes of the load current. Hence, the oxygen excess ratio is defined as the rate of oxygen supplied to the consumed.

For design of temperature control in the stack, the stack is regarded as a single thermal mass with a thermal capacity. Under the assumption that the heat exchange by radiation is negligible and the stack temperature is equal to the average of the stack outlet coolants temperature on the anode and cathode side, the variation of the temperature in the stack is equal to the sum of the heat source terms in the stack, the heat exchanged with the coolants.

$$mCp_{st} \frac{dt_{st}}{dt} = \dot{Q}_{sou} + W_c \cdot Cp_c \cdot (T_{c,in} - T_{st}) \tag{21}$$

where  $mCp_{st}$  is the heat capacity of the stack ( $J \cdot K^{-1}$ ),  $W_c$  is the coolant flow rate ( $kg \cdot s^{-1}$ ) as the control variable and  $\dot{Q}_{sou}$  is the internal energy source ( $J \cdot s^{-1}$ ) that is a function of the load current.

Due to the nonlinearity of the equations in the lumped thermal stack (Equation 21) and the reservoir model (Equation 19), Talyor's expansion is used for linearization at an operating point, where the reservoir temperature and coolant flow rate are set at 64°C and 0.93 kg/sec. The stack current and voltage are 140 A and 198 V, respectively. The state equations and variables are defined as follows:

$$\begin{aligned} \delta \dot{x} &= A \cdot \delta x + B_u \cdot u + B_w \cdot w \\ \delta y &= C \cdot \delta x \end{aligned} \tag{22}$$

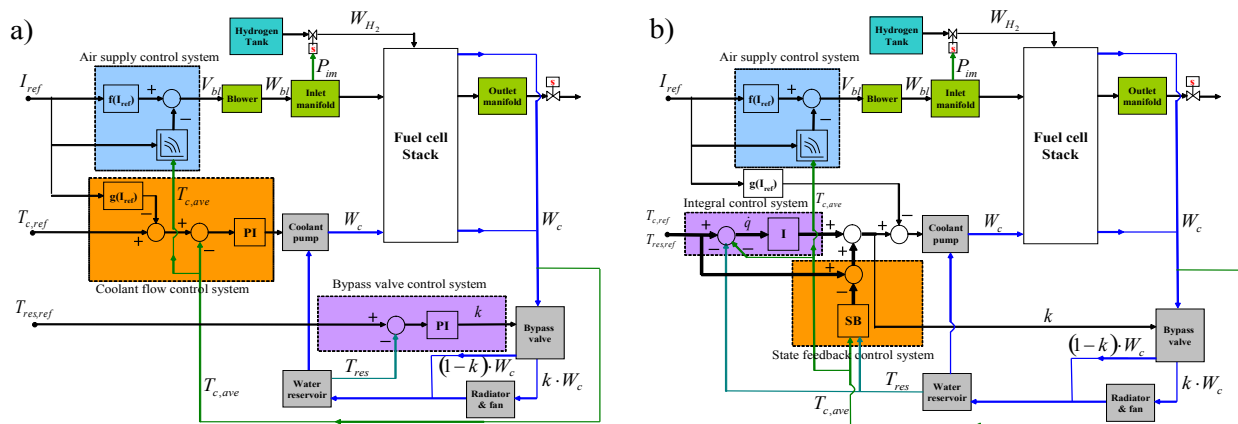


Figure 7: Block diagram for an air and coolant control with a) classic PI controllers and b) state feedback controller with integral controller

$$x = \begin{bmatrix} T_{st} & T_{res} \end{bmatrix} \quad (\text{States})$$

$$u = \begin{bmatrix} W_c & k \end{bmatrix} \quad (\text{Controlled input})$$

$$w = I_{st} \quad (\text{Disturbance})$$

$$y = \begin{bmatrix} T_{st} & T_{res} \end{bmatrix} \quad (\text{Output})$$

where the matrices of the linearized system, A, B<sub>u</sub>, B<sub>w</sub> and C, are listed in the Appendix.

### 2.5.1 DESIGN OF CLASSIC PI CONTROLS

The state equations derived above present a multi-input-multi-output structure, where two controlled input variables, coolant temperature and flow rate, are dependent on each other. This dependence can be minimized if the time constants of two feedback loops are set in a different order. Then the temperature in the stack can be controlled by the coolant flow rate independent of the temperature of the coolant being controlled by the opening factor k. Equation 21 includes a relationship between the stack temperature and the coolant flow rate, whose transfer function is given in Equation 23. The system shows the first order of the ordinary differential equation and thus a classic PI controller is employed. The two gains of the PI controller are selected by the bandwidth of the closed-loop that is 3 times higher than the time constant of the heat source term response, and a damping ratio of 0.707. The resulting gains are  $K_{p,c} = 0.25$  and  $K_{I,c} = 0.017 \text{ sec}^{-1}$ .

$$\frac{T_{st}(s)}{W_c(s)} = \frac{Cp_c \cdot (T_{res}^o - T_{st}^o)}{(mCp_{st} \cdot s + W_c^o \cdot Cp_c)} \quad (23)$$

$$G_{c1}(s) = K_{p,c} + \frac{K_{I,c}}{s} \quad (24)$$

Equation 19 includes a relationship between the temperature in the reservoir and the factor for the bypass valve opening, which the transfer function is given in Equation 25. Likewise, the gains for the PI controller are so selected that the bandwidth of the closed-loop is 5 times higher than the time constant of the coolant flow feedback outer loop. In addition, the damping ratio is set to be 0.707. The resulting gains are  $K_{p,b} = 0.1902$  and  $K_{I,b} = 0.0546 \text{ sec}^{-1}$ .

$$\frac{T_{res}(s)}{k(s)} = \frac{(W_c^o \cdot Cp_c + hA_{pl}) (T_{amb} - T_{st}^o)}{(mCp_{res} \cdot s + W_c^o \cdot Cp_c)} \quad (25)$$

$$G_{c2}(s) = K_{p,b} + \frac{K_{I,b}}{s} \quad (26)$$

### 2.5.2 DESIGN OF STATE FEEDBACK CONTROLS WITH INTEGRAL CONTROLS

The classic PI controllers do not consider the parasitic power in the coolant pump as a control object, even though it sufficiently rejects the heat and effectively suppresses the temperature surges in the layers. One alternative is the use of a state feedback control, where the parasitic power dissipated in the coolant pump can be advantageously considered as one of the control objectives [22]. On the other hand, the parasitic power of the coolant pump is directly proportional to the coolant flow rate. Thus, the coolant flow rate is included as a parameter in the cost function below. The optimization of the gains is conducted by the LQR (Linear Quadratic Regulator) method, which basically sums the square of the errors [17].

$$J = \int_0^{\infty} (\delta x^T Q_x \delta x + \delta u^T R \delta u) dt \quad (27)$$

where  $Q_x$  represents the weighting matrix amplifying the errors of the control objects, while the other weighting matrix R is used to suppress the effect of the manipulating variables.

The state equation of the control plant presents a 2-by-2 matrix, where the variables are coupled with each other. A decoupling of the two loops has been accomplished by assigning different time constants to the two closed loops. In fact, the valve opening factor does not directly affect the dynamics of the stack temperature, while the reservoir temperature is strongly influenced by the valve opening factor rather than the coolant flow rate. Hence, the time constant of the transfer function between the stack temperature and coolant flow rate is set 5 times faster than the one between the stack temperature and the valve opening factor.

On the other hand, integrators are required to suppress any steady state errors. Thus, the errors of both closed loops are defined as a new state variable that is considered in the cost function:

$$\dot{q} = \begin{bmatrix} T_{st}^* - T_{st} \\ T_{res}^* - T_{res} \end{bmatrix} \quad (28)$$

$$J = \int_0^\infty (\delta x^T Q_x \delta x + q^T Q_I q + \delta u^T R \delta u) dt \tag{29}$$

where  $Q_I$  is the weighting matrix for integrator.

Then, the rules for the optimal control inputs are obtained [23]:

$$\delta u = -K \begin{bmatrix} \delta x & q \end{bmatrix}^T = -K_p \cdot \delta x - K_I \cdot q \tag{30}$$

where the controller gain is  $K = R^{-1} B u^T P$ .  $P$  is the solution of the algebraic Riccati Equation that is given as follows:

$$P \cdot A' + A' \cdot P + Q - P \cdot B'_u \cdot R^{-1} \cdot B'^T_u \cdot P = 0 \tag{31}$$

where  $A', B'_u, Q = \text{diag}(Q_x, Q_I)$  and  $R$  is listed in the Appendix.

When the weighting matrix  $R$  is larger than the weighting matrix  $Q$ , the role of the coolant flow rate in the cost function increases, and subsequently, the gains of the controller are chosen, which minimizes the parasitic power. After several iterations with different weighting factors, the optimal control matrix  $K_p$  and  $K_I$  is given by

$$K_p = \begin{bmatrix} -1.2015 & 0.01 \\ -0.0521 & -3.1479 \end{bmatrix}, K_I = \begin{bmatrix} -0.1 & 0.0027 \\ -0.0027 & -0.1 \end{bmatrix} \tag{32}$$

### 2.6 Disturbance Compensation

The heat produced in the stack tends to follow the current drawn from the stack. The current-dependent heat is regarded as a disturbance in the control loop, which cannot be fully rejected by the typical coolant control that measures the temperature at the outlet of the coolants. As a result, the heat rejected gets less than the heat produced. A countermeasure is to estimate temperature rise in a layer that is directly related to the magnitude of the current load and feed-forward it to the temperature control loop shown in Figure 7. The relationship between the current and the stack temperature is derived by using Equations (5) and (21) which yields the following transfer function (Equation 33), where  $v_{act}$  represents the activation over-potential:

$$\frac{T_{st}(s)}{I(s)} = \frac{\left( -\frac{T\Delta s}{4F} + v_{act} \right)}{\left( m_{st} C p_{st} \cdot s + C p_c W_c^0 \right)}$$

$$\frac{T_{st}(s)}{I^2(s)} = \frac{R_{membr}}{\left( m_{st} C p_{st} \cdot s + C p_c W_c^0 \right)} \tag{33}$$

However, all of previously published air supply control designs assumed a constant working temperature of the cell [24]. In fact, distribution of the temperature in the individual layers through the plane varies because of the various heat sources of irreversible energy occurring in the chemical reactions, and Joule's losses associated with charges transport. In order for rejection of the heat in the stack to occur, the temperature of the coolant control loop is set lower than the one in the stack, thereby changing the temperature in the gas flow channels. When the temperature in the channel gets lower, the pressure drops according to the ideal gas law for the given volume, and then a pressure difference to the inlet manifold gets larger. On the other hand, the mass flow rate at the inlet of the stack increases according to the Nozzle equation [2] and consequently the oxygen excess ratio increases. The surplus air is reduced by an additional element in the controls that depends upon the coolant temperature in addition to the current that determines the consumed oxygen. Due to a nonlinear relationship between the blower voltage and different currents and temperatures at the optimum oxygen excess ratio, a set of data is obtained by multi-runs of the entire model under different currents and temperatures, used for a compensation of the effects.

### 3. SIMULATION AND ANALYSES

Simulations are performed to analyze the dynamic behavior of the stack along with the air supply, thermal system and the associated control strategies. Dynamics of water content in the membranes, temperature variations, oxygen excess ratio and responses at the load currents are analyzed in the following chapters. The parameters and reference data for the models chosen are as follows (Table 1), which are partially empirical [2], [8], [9], [25]. All models were coded by blocks given in MATLAB/Simulink.

Figure 8 shows a comparison of the membrane water content between the empirical model and the proposed model at a step load current. Primarily, the membrane water content depends on the relative humidity determined by the saturated vapor pressure which is dependent on the temperature and vapor pressures of the cathode and anode side. Since the empirical model assumed a constant temperature of 80°C in the membrane, no dynamics of water transfer are involved and subsequently the vapor pressure only follows the change of the load current. Conversely, the water balance in the membrane and the temperature strongly influence the water content in the membrane. The water content gets higher when the temperature of the catalyst layer on the cathode side is controlled at 80°C, and the temperature of the gas channel falls lower than 80°C. Then, the saturated vapor pressure decreases

Fuel Cell			Electrochemical Reation Model [2]		
n	381		P <sub>0</sub>	1.0	bar
A <sub>fc</sub>	0.028	m <sup>2</sup>	T <sub>ref</sub>	353.15	K
Proton Conducting Model [11]			E <sub>ref</sub>	1.229	V
b <sub>11</sub>	0.5139		A <sub>cat,eff</sub> /A <sub>cell</sub>	f(I, T, P <sub>O2</sub> )	
b <sub>12</sub>	0.326		Thermal model [9]		
b <sub>2</sub>	350		H <sub>gas</sub>	f(P, T)	
n <sub>d</sub>	f(C <sub>water</sub> )		C <sub>p, gas</sub>	f(P, T)	
D <sub>w</sub>	f(T, C <sub>water</sub> )		ρ <sub>gas</sub>	f(P, T)	
Gas Tranport Model [25]			Fr <sub>area</sub>	2	m <sup>2</sup>
De <sub>ff</sub>	f(P, T)		m <sub>res</sub>	5	kg
Psat	f(T)		hA <sub>pl</sub>	16.66	J K <sup>-1</sup>
Geometrical data for layers [9]					
	Thickness	Density	Heat conductivity	Specific heat	
	m	W m <sup>-1</sup> K <sup>-1</sup>	J kg <sup>-1</sup> K <sup>-1</sup>	kg m <sup>-3</sup>	
Coolant Channel	0.001	1400	30	935	
Plate	0.001	1400	52	935	
Gas Channel	0.001	1400	52	935	
GDL	0.0004	2000	65	840	
Catalyst layer	0.000065	387	0.2	770	
Membrane layer	0.000183	1967	0.21	1100	

Table 1: Simulation parameters

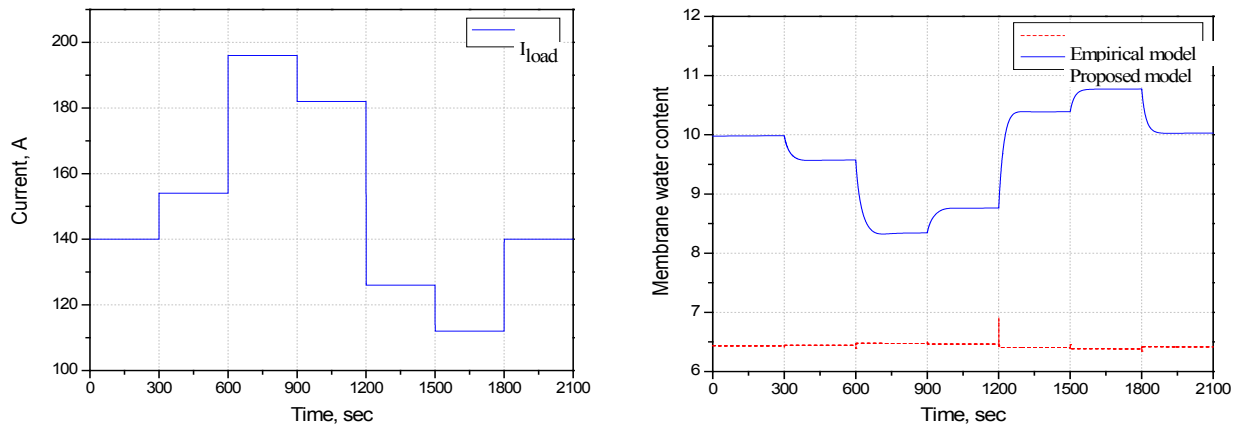


Figure 8: a) Current and b) water content in the membrane

and relative humidity becomes higher. It is observed that the elevated temperature of the stack by a high load current leads to a high saturated vapor pressure and a low relative humidity on both sides of the cell. As a result, the membrane water content is decreased.

### 3.1 Temperature, Water Content and Voltages in the Two-Cell Stack

Temperature in the catalyst and coolant channel with and without the feed-forward of the disturbance is shown in Figure 9. Due to the immeasurability of the temperature in the catalyst layer during operations, the actual temperature is usually measured at the stack outlet coolants on the anode and cathode sides, and then averaged. Considering the maximum limit of the temperature in the catalyst and membrane, a reference temperature for the coolant control is set to be 76°C.

When a multi-step current is applied to the stack, the temperature in the stack rapidly rises, particularly in the catalyst on the cathode side. The temperature rise is 3~7°C higher than the average temperature in the stack, where the coolant temperature is fully controlled for the reference temperature 76°C (see Figure 9). It should be noted that the catalyst and membrane layers could be overheated and damaged.

The difference in temperature in the layers can be reduced by a feed-forward (FF) of the disturbance to the coolant control loop that should reject this excessive heat as quickly as possible. The transfer function of the disturbance is given in Equation 23. The result of the control strategy proposed is illustrated in Figure 9 with a straight line, where the temperature of the catalyst layer is nearly maintained at 80°C. The coolant temperature keeps track of the variation in the catalyst temperature. However, an instant rise in temperature cannot be fully suppressed because of the high thermal mass and large heat capacity of the stack. In addition, there remains a steady state error caused by the temperature difference between the coolant channel measured and the catalyst layer. Nevertheless, the cooling of the cell is effective and the duration of the heat on individual layers can be minimized.

Effects of the coolant controls on temperature distributions through the plane of a cell are shown in Figure 10. As the amplitude of the current changes stepwise from 0.5 to 0.55 A, 0.65 A and 0.7 A, the stack temperature accordingly becomes higher. When the feed-forward is applied, the overall stack temperature is lowered and the catalyst temperature is kept at 353.5 K, which is significantly lower than before. Likewise, the maximum difference of the temperature between the catalyst on the cathode side and the coolant channel

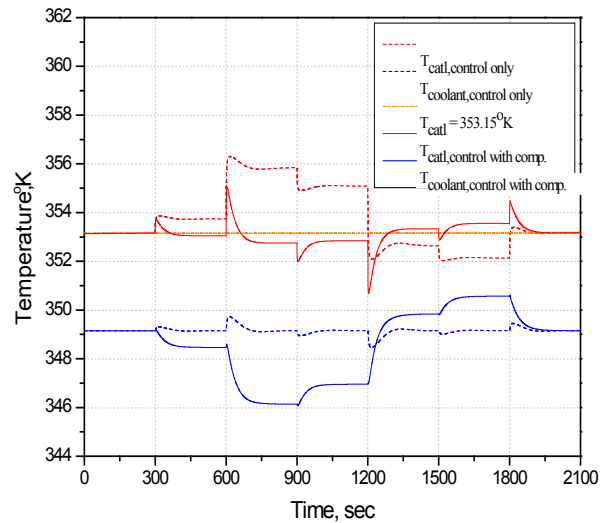


Figure 9: Temperatures of the catalyst layer and coolant channel by the coolant flow controls

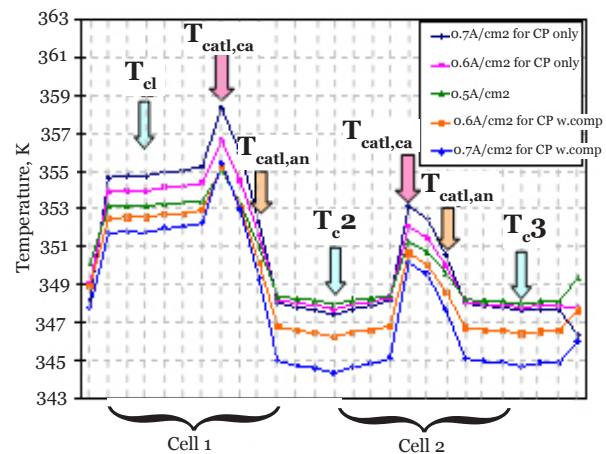


Figure 10: Temperature distribution in a two-cell stack with and without the feed-forward of the disturbance

becomes 4K lower than before. As a result, the cooling of the stack becomes more effective than before.

In fact, the proton conductivity in the membrane depends on the water content and temperature. High proton conductivity reduces the ohmic over-potential and subsequently the cell voltage is increased. In addition, the water content in the membrane and the temperature of cell 1 is higher than that of cell 2, as shown in Figure 11a. Consequently, the voltage of cell 1 becomes higher than that of cell 2 as shown in Figure 11b. The dynamic behavior of the stack voltage follows the dynamics of the water content in the membrane.

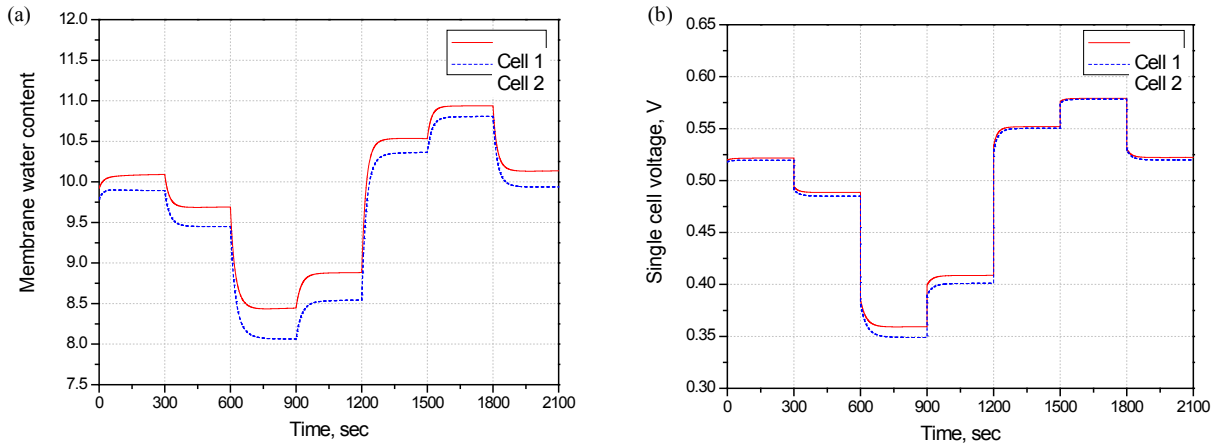


Figure 11: Dynamic behavior of (a) membrane water content and (b) individual cell voltages

### 3.2 Oxygen Excess Ratio

Oxygen excess ratio is illustrated in Figure 12 at a constant and dynamically varying temperature with a coolant flow control. Due to the change of pressure in the gas flow channel caused by variations in the stack temperature, the oxygen excess ratio is inversely influenced by the direction of the current changes.

Figure 13 shows a comparison of the oxygen excess ratio before and after a compensation of the temperature influence on the air control loop. The compensation enables the oxygen excess ratio to be maintained at level 2, even though the current applied to the stack varies stepwise, which implies that the parasitic power at the blower gets less.

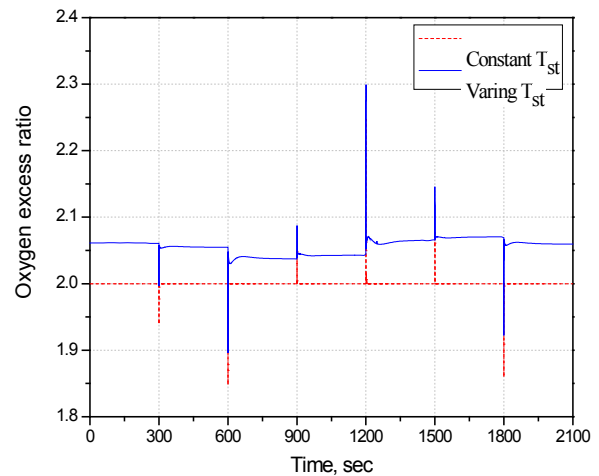


Figure 12: Comparison of oxygen excess ratio at a constant and varying temperature

### 3.3 Comparison of the PI and State Feedback Controls

Comparison between both controls shows that the parasitic power of the state feedback controls a multi-step current load is 5% less than the one by the PI controls. However, the dynamic response is much improved by the state feedback controls. In Figure 14, step responses of two controls are simulated with the models aforementioned. The output states are the coolant flow rate and the stack inlet coolant temperature. The rise time of the coolant flow rate by the state feedback controller is 6 seconds, is 4 times faster than the one by PI controls. Likewise, the rise time of the stack inlet coolant temperature is 3 times faster than the one of the PI controllers.

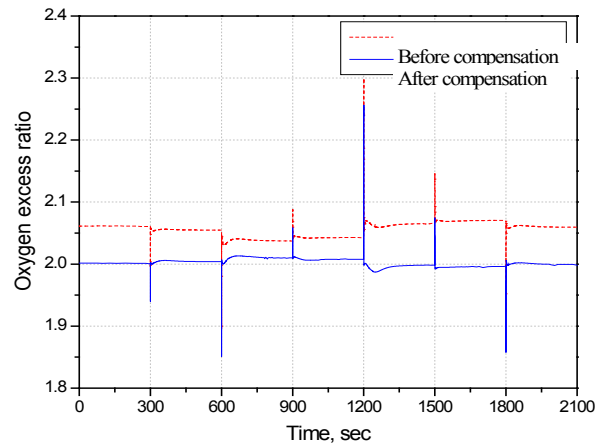


Figure 13: Comparison of the oxygen excess ratio a) before, b) after temperature compensation

Parasitic power is calculated by summing up the electrical power necessary for driving the blower and the coolant pump. The control strategies with the

state feedback control proposed require 100 kW at the multiple step current, while the one without the considering valve and PI control loop for the coolant needs 106 kW.

Furthermore, the response of the state feedback control is compared with a conventional one by using a current profile obtained from a vehicle tested at the Federal Urban Driving Schedule (FUDS). Figure 15 shows the simulation results for the two different control strategies at the current. The peak temperature in the catalyst layer is 6°K higher than the working stack temperature by the control without the FF, even though the coolants are fairly controlled around the set reference temperature shown in Figure 15b. Figure 15c shows the temperature of the catalyst and coolants with the FF of the disturbance. The peak of the temperature is similar to the others for the first 200 seconds, but is substantially suppressed in the following intervals compared to Figure 15b. The excursion duration of the catalyst temperature lessens, and the heat energy imposed on the thin layers can finally be reduced, which significantly reduces the heat stress on the layers. Correspondingly, the oxygen excess ratio is fairly maintained at the optimum value by the compensation

shown in Figure 15d.

#### 4. CONCLUSION

The paper describes a dynamic simulator that represents behavior of a stack and the design and analysis of air and coolant flow controls that affect dynamics and performance. Particularly, the model includes gas diffusion in the GDL, dynamic water balance in the membrane and temperature variation in the cells, and components of air supply and thermal system temperature effects and the controllability is assessed. The major outcomes are summarized as follows:

- o Highly dynamic stack behavior is accomplished by adding dynamic water balance in the membrane and through a partial pressure drop in the GDL and temperature distributions. The results show that distribution of the temperature through the plane is asymmetric and the temperature rise amounts to 3-7°C, potentially damaging the layers at a high current load. Therefore, proper control of the temperature might be required to secure durability and increase efficiency.
- o Most control strategies have focused on

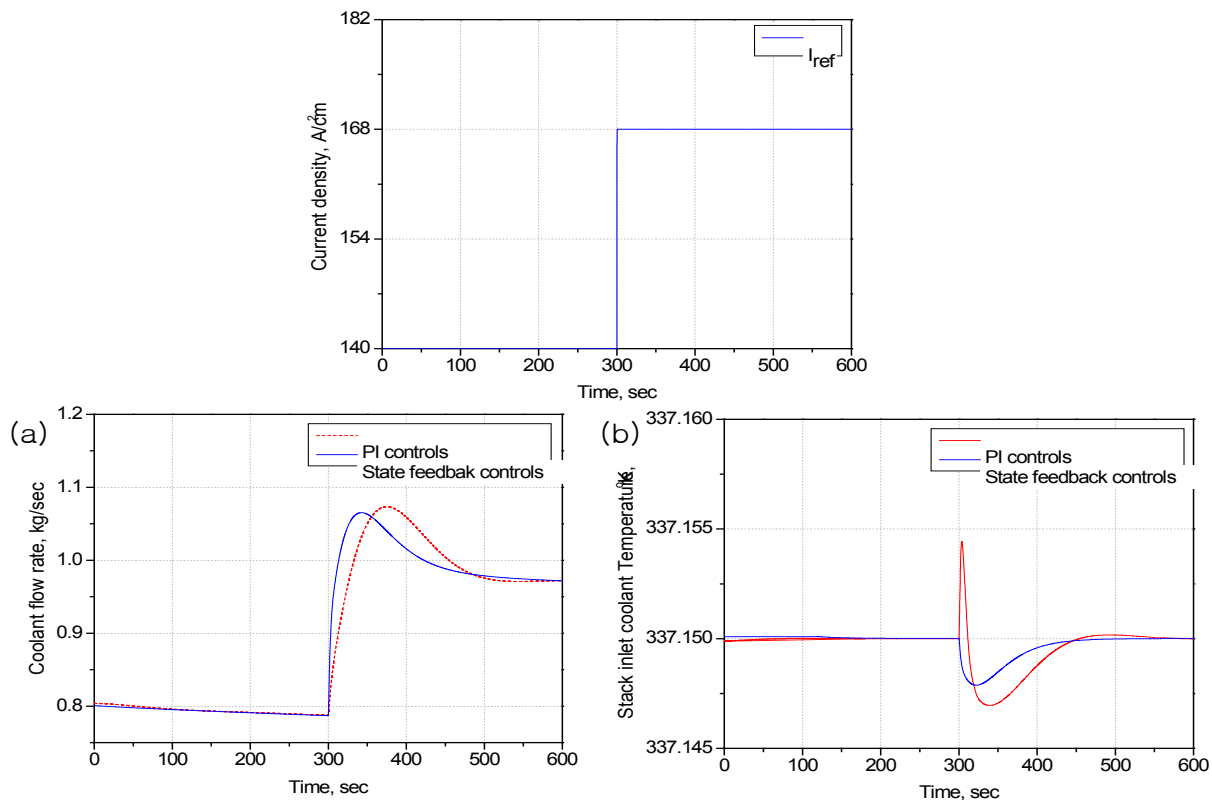


Figure 14: Comparison of a) coolant flow rate and b) stack inlet coolant temperature with a given current step between PI controls and state feedback controls

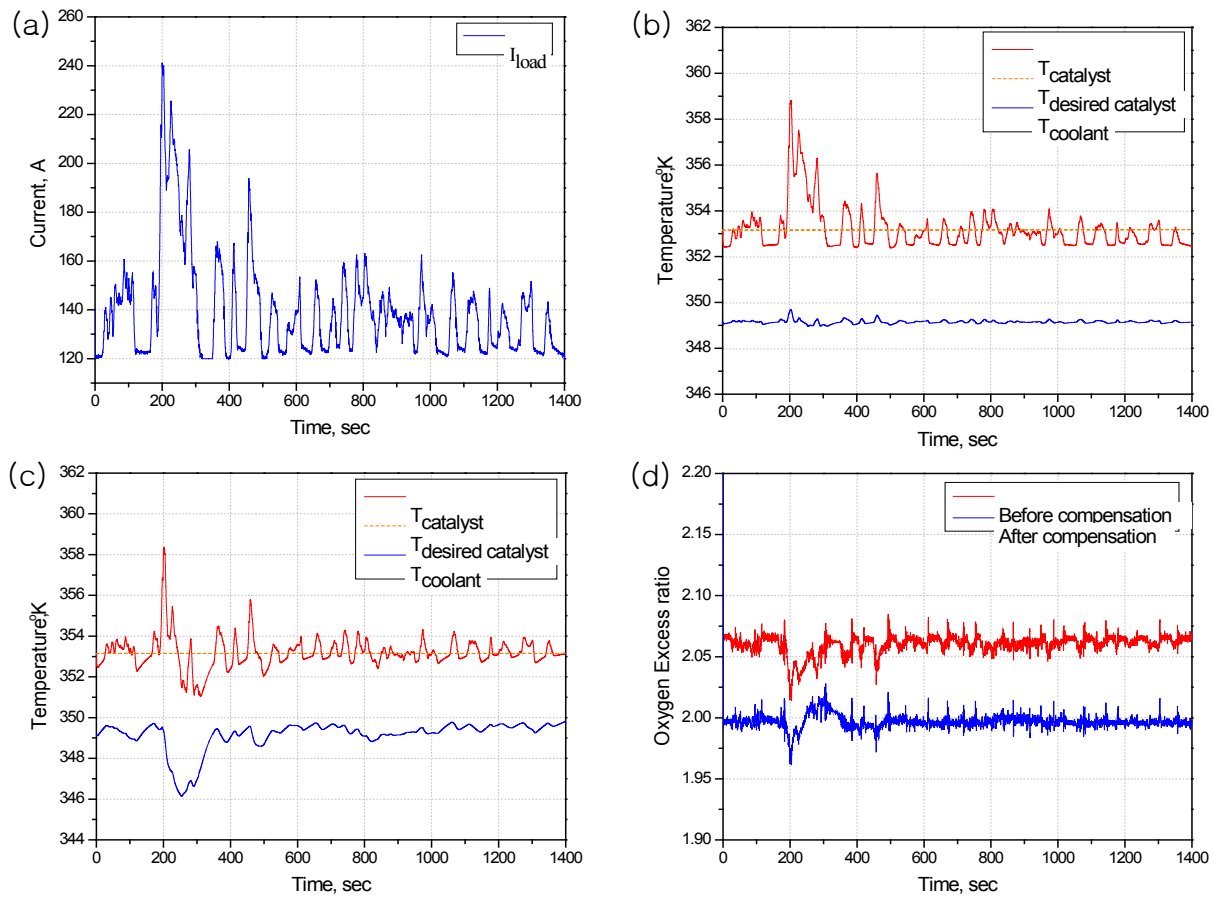


Figure 15: (a) FUDS and a current profile with a base load of 120 A, (b) temperature of the catalysts and coolants without the FF, (c) temperature of the catalysts and coolants with the FF, and (d) oxygen excess ratio after a temperature compensation

optimization of the air supply system, where the working temperature in the stack is presumed to be constant. However, it turns out that the oxygen excess ratio inversely varies as the temperature changes. Thus, the ideal oxygen excess ratio necessary for prevention of an oxygen starvation cannot be maintained at the optimum value of 2.

o New control strategies include a state feedback control with a feed-forward of the disturbance and a compensator for minimization of the temperature effect on the air flow rate. For the design of the temperature controller, the thermal circuit is approximated with a second order system. Classic PI and state feedback controls are designed to compare the effectiveness of the cooling. The results show that the temperature rise in the catalyst can be kept within an allowable value and duration. In addition, the oxygen excess ratio can be maintained with an optimal value by minimizing the influence of temperature variations in the gas flow channel. Consequently,

the power consumption of the blower can be reduced by more than 15% by compensation, and 5% by the controlling bypass valve at a multi-step load profile. Final reduction of the total parasitic power has been accomplished by approximately 7%.

**APPENDIX**

$$A = \begin{bmatrix} -0.0245 & 0.0245 \\ 0.0243 & -0.0487 \end{bmatrix}, B_u = \begin{bmatrix} -0.3179 & 0 \\ 0.0089 & -1.1482 \end{bmatrix}, B_w = \begin{bmatrix} 0.634 \times 10^5 \\ 0 \end{bmatrix}, C = \begin{bmatrix} 1 & 0 \\ 0 & 1 \end{bmatrix}$$

$$A' = \begin{bmatrix} -0.0245 & 0.0245 & 0 & 0 \\ 0.0373 & -0.0488 & 0 & 0 \\ 1 & 0 & 0 & 0 \\ 0 & 1 & 0 & 0 \end{bmatrix}, B'_u = \begin{bmatrix} -0.3179 & 0 \\ 0.0089 & -2.4756 \\ 0 & 0 \\ 0 & 0 \end{bmatrix}, Q = \begin{bmatrix} 10 & 0 & 0 & 0 \\ 0 & 1 & 0 & 0 \\ 0 & 0 & 0.01 & 0 \\ 0 & 0 & 0 & 0.01 \end{bmatrix}$$

$$R = \begin{bmatrix} 100 & 0 \\ 0 & 1 \end{bmatrix}$$

## REFERENCES

- [1] W.C. Yang, B. Bates, N. Fletcher, and R. Pow, Control challenges and methodologies in fuel cell vehicle development, SAE Paper 98C054, 1998.
- [1] J.T. Pukrushpan, H. Peng, and A.G. Stefanopoulou, Simulation and Analysis of Transient Fuel Cell System Performance based on a Dynamic Reactant Flow Model, Proc. of IMEXE'01, ASME International Mechanical Engineering Congress & Exposition, New Orleans, LA., 2002.
- [3] H. Galip H. Guvelioglu and Harvey G. Stenger, Computational fluid dynamics modeling of polymer electrolyte membrane fuel cells, *J. Power Sources*, 147 1-2 95-106, 2005.
- [4] S. Um, C.Y. Wang, Computational fluid dynamics modeling of proton exchange-membrane fuel cells, *J. Electrochem. Society*, 147 4485-93, 2000.
- [5] L. Ma, D.B. Ingham, M.C. Pourkashanian, E. Carcadea, Review of the computational fluid dynamics modeling of fuel cells, *Journal of Fuel Cell Science and Technology*, 2 4 246-57, 2005.
- [6] Y. Shan and S.Y. Choe, A High Dynamic PEM Fuel Cell Model with the Temperature Effects, *J. Power Sources*, 145 30-39, 2005.
- [7] P.C. Krause and O. Wasynczuk, *Electromechanical Motion Devices*, first ed., McGraw-Hill Book Company, New York, 1989.
- [8] M. Ceraolo, C. Miulli and A. Pozio, Modeling static and dynamic behaviour of proton exchange membrane fuel cells on the basis of electro-chemical description, *J. Power Sources*, 113 131-144, 2003.
- [9] S. Gurski, Cold Start Effects on Performance and Efficiency for Vehicle Fuel Cell System, Master of Science Thesis, Virginia Polytechnic Institute and State University, 2002.
- [10] M. WÖhr, K. Bolvin, W. Schnurnberger, M. Fischer, W. Neubrand and G. Eigenberger, Dynamic modeling and simulation of a polymer membrane fuel cell including mass transport limitation, *Int. J. Hydrogen Energy*, 23 3 213-218, 1998.
- [11] J.C. Amphlett, R.M. Baumert, R.F. Mann, B.A. Peppley, and P.R. Roberge, Performance modeling of the Ballard Mark IV solid polymer electrolyte fuel cell, *J. Electrochem. Soc.*, 142 1 9-15., 1995.
- [12] Y. Shan, Dynamic modeling of polymer electrolyte membrane Fuel Cell Stack with 1D and 2D CFD Techniques, Master of Science Thesis, Auburn, 2006.
- [13] S. Gelfi, A.G. Stefanopoulou, J.T. Pukrushpan, and H. Peng, Dynamics of Low-Pressure and High-Pressure Fuel Cell Air Supply Systems, Proceedings of American Control Conference, Denver, Colorado, 2003.
- [14] R.T. Meyer, and B. Yao, Modeling and Simulation of a Modern PEM Fuel Cell System, Proceedings of Fuel Cell 2006, Irvine, CA, June, 2006.
- [15] Phoenix Design & technologies, The PDAT Turbomix, <http://www.padtinc.com/sales/fuelcell/turbomix/>, March 2007.
- [16] J.T. Pukrushpan, A.G. Stefanopoulou, and H. Peng, Control of Fuel Cell Breathing, *IEEE Control System Magazine* 24 2 30-46, April 2004.
- [17] B.D.O. Anderson, and J.B. Moore, *Optimal control: Linear Quadratic Methods*, Prentice-Hall, NJ, USA, 1989.
- [18] D.G. Kroger, Radiator Characterization and Optimization, SAE paper 840380, 1984.
- [19] A.D. Domenico, A. Miotti, M. Alhetairshi, Y.G. Guezennec, S.S.V. Rajagopalan, and S. Yurkovich, Multi-variable control for an automotive traction PEM fuel cell system, Proc. the 2006 American Control Conference, Minneapolis, Minnesota, 2006.
- [20] P. Rodatz, G. Paganelli, and L. Guzzella, Optimization air supply control of a PEM Fuel Cell system, *IEEE Proc. American Control conference*, 2003.
- [21] A. Vahidi, A.G. Stefanopoulou, and H. Peng, Model Predictive Control for Starvation Prevention in a Hybrid Fuel Cell system, *IEEE Proc. American Control conference*, 2004.
- [22] J.W. Ahn, Design and Analysis of Air and Coolant Control for a Polymer Electrolyte Membrane Fuel Cell, Master of Science Thesis, Auburn, 2007
- [23] M. Grujicic, K. Chittajallu, and J.T. Pukrushpan. Control of the transient behavior of polymer electrolyte membrane fuel cell systems, *Proc. Intl. Mech. Engrs*, 218D, 2004
- [24] M. Sundaresan, A Thermal Model to Evaluate Sub-Freezing Startup for a Direct Hydrogen Hybrid Fuel Cell Vehicle Polymer Electrolyte Fuel Cell Stack and System, Ph.D. in Transportation Technology and Policy, UC Davis, 2004.
- [25] T.E. Springer, T.A. Zawodzinski, and S. Gottesfeld, Polymer Electrolyte Fuel Cell Model, *J. Electrochem. Soc.*, 138 8 2334-2342. 1991.

## AUTHOR



Dr. Song-Yul (Ben) Choe, Associate Professor of Mechanical Engineering at Auburn University, earned his Ph.D. in Electrical Engineering from the Technical University of Berlin (1991). Before teaching at Auburn, he was a program manager and research professor at the Center for Advanced Vehicular Systems at Mississippi State University, by leading efforts on the fuel cell and the advanced intelligent vehicle. From 1996 until 2001, he worked as a director overseeing advanced automotive technology at Hyundai Corporation. He has experience in advanced propulsion systems and associated controls for vehicles, and has published over 50 technical papers.